Low-tortuosity water microchannels boosting energy utilization for high water flux solar distillation

Ying Xu,[†] Chuyang Tang,[‡] Jiaxiang Ma,[†] Dongqing Liu,[†] Dianpeng Qi,[†] Shijie You,[†] Fuyi Cui,[§] Yen Wei,[‖] Wei Wang*,[†]

[†]State Key Laboratory of Urban Water Resource and Environment, School of Environment, Harbin Institute of Technology, Harbin 150090, China.

[‡] Department of Civil Engineering, The University of Hong Kong, Pokfulam HW619B, Hong Kong, China

[§]College of Urban Construction and Environmental Engineering, Chongqing University, Chongqing 400000, China.

[‖]MOE Key Laboratory of Bioorganic Phosphorus Chemistry & Chemical Biology, Department of Chemistry, Tsinghua University, Beijing 100084, China.

14 **ABSTRACT**

15 Solar distillation through photo-thermal evaporators has approached solar light energy

16 (E_1) limit under no solar concentration, but still suffers from modest vapor and clean

17 water production. Herein, a nature-inspired low-tortuosity 3D evaporator is

18 demonstrated to significantly improve water production. The solar evaporator, prepared

19 from polypyrrole-modified maize straw (PMS), had upright vascular structures

20 enabling high water lifting and horizontal micro-gaps facilitating broad water

21 distribution to the out-surface. Consequently, this novel PMS evaporator dramatically

22 enhanced the utilization of the heat energy stored in the environment (E_2) for promoting

23 evaporation. The maximum vapor generation rate of a single PMS respectively

24 increases 2.5 times and 6 times compared with the conventional 3D evaporators and the

25 planar evaporators of identical occupied area. Consequently, a scaled-up PMS array

26 achieved a state-of-the-art vapor generation rate of $3.0 \, \mathrm{L \, m^{-2} \, h^{-1}}$ (LMH) under simulated

27 condition and a record-high clean water production of 2.2 LMH for actual seawater

28 desalination under natural conditions (one-sun intensity). This breakthrough reveals

29 great potentials for cost-effective freshwater production as well as the rational design

30 of high-performance photothermal evaporators for solar distillation.

31

32   **TOC Art**

Planar system   Conventional 3D cylinder   PMS with low-tortuosity

33
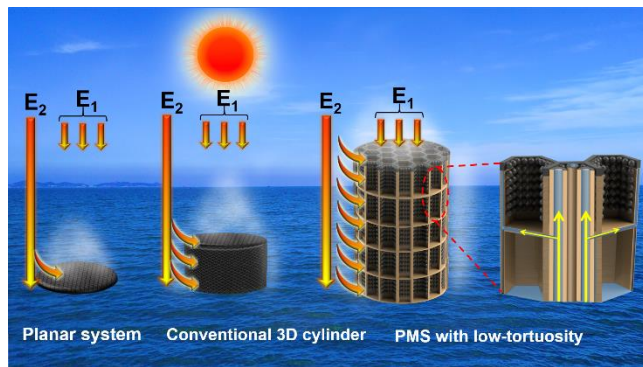
1. INTRODUCTION

Solar distillation, as a direct utilization technology of solar energy, holds immense potential in fresh water production, water treatment, power generation and so on.[1-4] In particular, it is one of the most promising approaches for water purification in remote areas and in some emergency circumstances where access to centralized drinking water supply or electricity is unavailable.[5, 6] Solar distillation relies on the photothermal evaporators to adsorb and convert light energy to localized heat to driven steam generation and transportation.[7-10] So far, researchers have been mainly focusing on the development of photothermal evaporators with broadband solar spectrum absorption capacity, excellent thermal insulation and super-hydrophilicity to improve the efficiency of solar light energy utilization.[11-18]

However, a critical bottleneck of solar distillation is the low theoretical value of vapor-producing flux (1.4 L m^{-2} h^{-1}, LMH) under one sun irradiation (1 kW m^{-2}), even if the light energy is totally absorbed and transferred into the vapor.[19-21] Researchers found that reducing the enthalpy of water through novel material design can potentially improve water production.[22-26] Nevertheless, the requirement of forming the porous structure in hydrogel under harsh condition (e.g. repeated freeze thawing in liquid-nitrogen) prevents the economical scaling up of this technology. An alternative approach should be to develop much more facile and economical strategies to break through the limitation of water production.

In the actual operation of a solar evaporator, two parts of energy can contribute to

the evaporation of water (Figure 1): (1) the light energy (E_1) that irradiates on the confined evaporator surface, which is converted to localized heat energy by the photothermal materials; (2) the heat energy (E_2) that is stored in the environment, which determines the environmental temperature.[27] In traditional 2D planar evaporation, E_1 is the main driver for vapor generation. Three-dimensional (3D) evaporators can enhance evaporation by capturing E_2. Theoretically, increasing the height of water transport in a 3D evaporator can promote better utilization of E_2. Nevertheless, the evaporation enhancement contributed by E_2 (EC_{E2}) for conventional 3D evaporators is generally less than 40%, which is largely limited by capillary water lifting and distribution capacity.[28-33]

Nature provides us an inspiring solution. The vascular bundle structure of maize straws (MS, an agricultural waste) features low-tortuosity water micro-channels. Serve as the aorta of the plant, these straight microchannels can transport water from the bottom soil to dozens of meters high and then distribute water horizontally through the micro-gaps connected to vascular.[34-36] Inspired by the outstanding ability of MS water channels to transport and distribute water, we prepared a highly efficient 3D solar evaporator using a simple chemical decoration of MS by polypyrrole (PPy) (denoted as PMS). The simultaneous actions of efficient vertical capillary water lifting by the straight vascular structures and the horizontal water transport to the outside surface through its micro-gaps enabled a single PMS to achieve an outstanding solar-to-vapor efficiency of 91.3% through E_1 and high vapor production of 10.3 LMH by the

76 enhancement of E_2. When forming an array, the vapor production still reached a state-

77 of-the-art value of 3.0 LMH with an EC_{E2} of approximately 106% by reducing the

78 interaction among each evaporation field of individual PMS straws. A prototype of

79 optimized PMS array exhibited a vapor production rate of 2.2 LMH (normalized to one-

80 sun intensity) for actual seawater desalination under natural condition, which is 4 times

81 that of a planar photothermal system, highlighting its great potential for practical

82 applications.
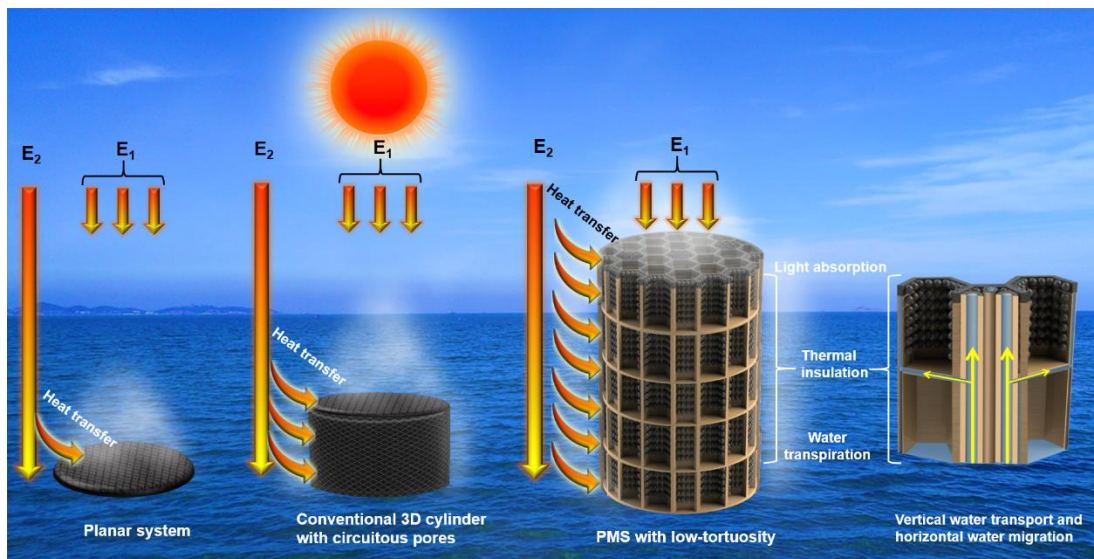
83

84 Figure 1. The schematic illustration of the solar energy utilization among typical planar system,

85 conventional 3D cylinder with circuitous pores and PMS with low-tortuosity in water

86 evaporation.

87 **EXPERIMENTAL SECTION**

88 **Fabrication of PMS.** The MS was first immersed in the homogeneous Py monomer (2

89 g/L) aquatic solution for pre-absorption. Afterward, the $FeCl_3 \cdot 6H_2O$ (8 g/L) as oxidant was

90 added into the above solution to start the chemical polymerization of PPy. After 1 h of

6

91 polymerization, the obtained PMS was washed with DI water and dried at room temperature.

92 The detailed chemicals and procedures provided in the section 1, SI.

93 **Solar distillation experiment**. The as-prepared samples were stabled by Expandable

94 polyethylene (EPE) foams with their underparts immersing in DI water. In this case, the water

95 surface was totally covered by the EPE foam, without exposed area. Then, the solar distillation

96 was operated in both simulated condition in lab and natural condition under sun. The vapor

97 generation rates were calculated as the mass-change of feedwater balanced by an electronic

98 balance, while the clean water production rate under real sun was determined by the weight of

99 the collected distilled water. The detailed procedures, characterizations and other experimental

100 information were all provided in the SI.

101 **RESULTS AND DISCUSSION**

102 **Fabrication and morphologies**. The fabrication process of the PMS was facile

103 and easily scaled-up attributing to mild reaction conditions. As illustrated in Figure 2A,

104 the MS cut from a maize plant (without shell) was immersed in the homogeneous Py

105 solution with oxidant. After polymerization, the MS cylinder presented a black

106 appearance owing to the coverage of PPy particles, revealing an enhancement of light

107 absorption.[37] Strong interactions and connections between PPy particles and MS matrix

108 were expected due to that Py was able to bound to native substance via the hydrogen

109 bonding between –N on Py rings and – OH of cellulose.[38] The result of Fourier

110 transform infrared spectroscopy (FT-IR) demonstrated the existence of abundant – OH

111 groups in pristine MS and additional signals of C–N stretching vibration bands of PPy

112 (Figure S1), indicating the successful coating.[39, 40] Figure 2B shows the PMS consisted

113 of honeycomb cell structures layer-by-layer and vascular bundle structures along with

114 tracheid. After polymerization, the hexagonal structures on the top layer were well

115 preserved (Figure 2C) and the PPy nanoparticles were found symmetrically anchored

116 on the surface of the cell walls (Figure 2D). The average diameter of the tangent circles

117 of these hexagons was $\approx$ 100 μm (ranging from 20 to 200 μm, Figure S2A) and the

118 thickness of the robust cell wall was $\approx$ 0.3 μm (Figure S3A). The cross-section of the

119 core consisted of rectangular square boxes and vascular bundles for water transportation

120 and storage (Figure 2E and F). Coincidentally, the average height of the honeycomb

121 box layer was also 100 μm (ranging from 35 to 200 μm in Figure S2B), indicating the

122 regularity of its cell arrangement. The vascular bundle consists certain tubulars with no

123 diaphragm for rapid water lifting. The diameters of the tubulars were ranging from 10

124 to 200 μm and the heights of tubulars corresponded to the height of the stem (Figure

125 2E and S3B). As a masterpiece of nature, this perfect structure of the PMS played an

126 essential role in the rapid and uniform water transport in plants, which also made sense

127 in light absorption and heat insulating over solar distillation.
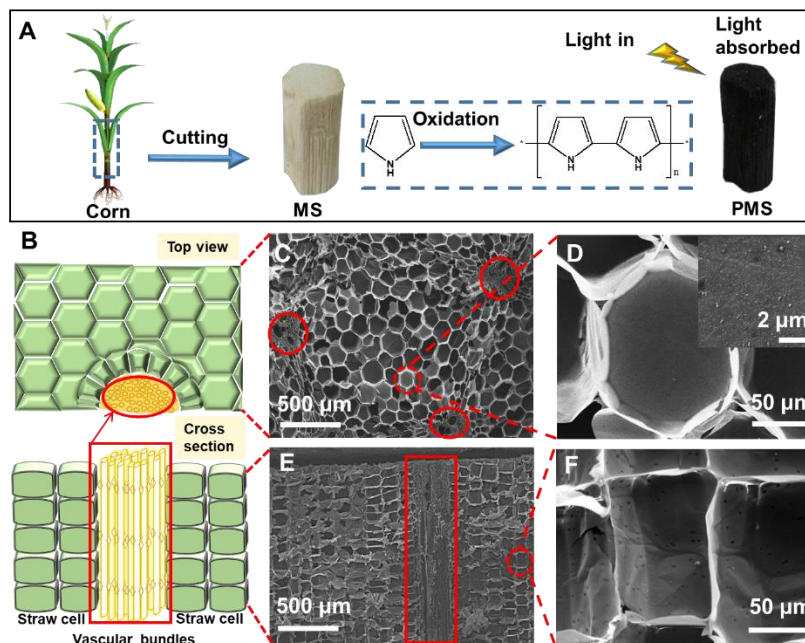
Figure 2. Fabrication and morphologies of the PMS. (A) The graphical illustration of the polymerization process of the PMS. (B) Schematic illustration of the structure of the top view and cross-section view of the PMS. SEM images of (C) the top view of the PMS and (D) the magnified image of a whole cell. The inset shows the magnification of the PPy coated cell wall. SEM images of (E) the cross-section view of the PMS and (F) the magnified image of a whole cell.

The optical absorption capacity as an essential property of solar evaporator was measured by an ultraviolet–visible–near infrared (UV−Vis–NIR) spectrophotometer from 250 - 2500 nm equipping with an integrating sphere (Figure 3A). Taking energy distribution of the solar spectrum into account (AM 1.5 G, grey line in Figure 3A), the average solar energy absorption rate of PMS was ultimately calculated to be 97.5%. This dramatic high value was attributed to the broadband capacity of PPy nanoparticles and the low reflection of the honeycomb structures at surface. The compressive capacities of the as-prepared samples were tested by a universal testing machine as

142 shown in Figure 3B. For comparison, the pristine MS was also treated at 500°C in Ar

143 for 1 h to obtain the carbonized MS.[25] As shown in Figure S4, the volume of the PMS

144 increased 5 - 8% after polymerization, in the meanwhile, the carbonized MS shrank

145 about 40% in comparison with the pristine MS. Correspondingly, the compressive stress

146 of the PMS was increased to 0.8 MPa, which is higher than that of the pristine MS (0.7

147 Mpa) and carbonized MS (0.2 MPa), indicating that the polymerization process

148 enhanced the mechanical strength of the PMS.

149 Since the solar evaporator was filled up with water during evaporation, it is

150 important to understand its properties under a wet state. First, the water absorption

151 capacity of the PMS was 579 wt%, which is lower than that of the pristine MS (759%)

152 due to that the swelling property of cellulose was weakened by PPy coating (Table S1).

153 The thermal isolation of the wetted evaporator was measured using a laboratory-built

154 test-apparatus and captured by IR camera (Figure S5). The thermal conductivity of the

155 wet PMS was calculated to be 0.3909 W m^{-1} K^{-1}, which is lower than that of water

156 (0.6000 W m^{-1} K^{-1} at room temperature), indicating that the heat generated from solar

157 illumination can be effectively localized in PMS instead of being transported to the

158 underneath bulk water. The wettability of the samples was shown in Figure 3D. The

159 water drop was immediately absorbed by the cores of MS and PMS within 2 s,

160 indicating the superhydrophilicity (water contact angle (WCA) is 0°). Four dry PMS

161 cylinders (10-cm-height) with different diameters was conducted to optimize the water

162 transportation (Figure S6A). Once in touch with water, the dynamic temperature

163 variations of the cylinders were captured by an infrared (IR) camera. As shown in

164 Figure S6B, the larger the diameter of PMS is, the lower the height of water that can be

165 transported. Only PMS with a diameter around 1.5 cm can be transported to a height of

166 10 cm. It is reasoned capillarity of the vascular bundle is weaker in the PMS with larger

167 area (detailed in Figure S7). Hence, the sample with diameter of around 1.5 cm was

168 chosen as the optimized evaporator.
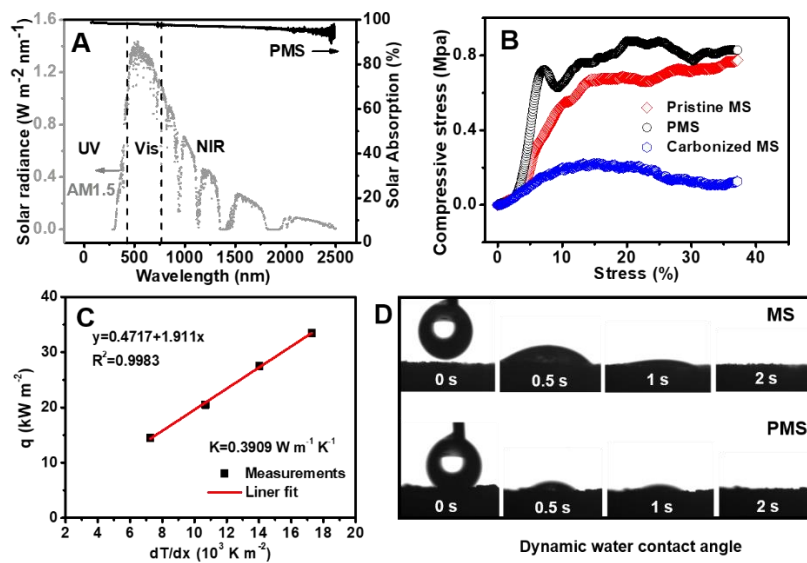
169

170 Figure 3. Optical behaviors and water transportation of PMS. (A) The solar spectral irradiance (AM

171 1.5 G) (gray, left side axis) and solar absorption (black, right side axis) of the PMS. (B) Compressive

172 stress-strain curve of the MS, PMS and carbonized MS.

173 **Solar evaporation experiments.** A single PMS cylinder as a 3D solar evaporator

174 could vaporize 10.3 LMH steam (based on the occupied area) by concurrently energy

175 utilization of both E_1 and E_2. The solar evaporation capacity of the upper surface of

176 PMS under a 2D state was systematically evaluated to test its utilization of E_1. Typical

177 mass-change curves of the upper surface under different conditions were plotted in

11

178   Figure 4A. Upon illumination, the water at the upper layer, absorbed by the capillarity

179   of the PMS, vaporized to steam as a result of the photo-thermal conversion. The whole

180   evaporation rate of the upper layer was calculated to be 1.69 LMH under one-sun

181   illumination, which was 3.4 times that of the upper layer without E_1 irradiation (0.51

182   LMH). In contrast, the evaporation rate of the pure water under illumination without

183   solar evaporator was only 0.4 LMH, resulting from its poor light-absorb capacity. The

184   dynamic heat distribution and transfer over the PMS system were recorded by IR

185   thermal imager, meanwhile, the maximum temperatures (T_{max}) and average

186   temperatures (T_{ave}) of the upper layer were plotted as a function of time (Figure 4B).

187   Attributing to the water infiltration and evaporation, the T_{ave} at the upper surface of the

188   PMS without E_1 is 3.4°C lower than the room temperature (19.6°C). Only 20 s after

189   illumination, the T_{ave} and T_{max} increased by about 10 and 11.2°C compared with the

190   original temperature. The thermal equilibrium of the system reached after 120s and

191   lasted for an hour, and the T_{max} and T_{ave} at equilibrium were $\approx$ 36.8 and 34.3°C,

192   respectively. The temperature of the bulk water increased from 19.6°C to 21.4°C due

193   to the heat conduction loss from the PMS. Above results demonstrated that the PMS

194   can effectively covert the E_1 into heat so as to improve the efficiency of light - vapor

195   conversion under direct illumination. The solar-to-vapor efficiency of E_1 was calculated

196   to be of the upper layer was calculated to be 81.6 ± 4.52% with a power density of 1

197   kW m^{-2},(detailed in Section 3, SI) which is a relatively high value among early reports

198   due to its low heat consumption.[38, 39] Moreover, the evaporation rate of the upper layer

199   under 3, 5, 7, and 10 Sun were calculated to be 4.37, 7.20, 10.00, and 14.31 LMH,

200   respectively. Accordingly, the light-to-vapor efficiencies of the upper layer under

201   various illuminations are calculated to be 89.6%, 93.8%, 95.6% and 97.8% under 3, 5,

202   7, and 10 Sun (Figure S8). The remarkable light-to-vapor conversion efficiencies of the

203   upper layer of PMS should be attributed to the unique natural structure, broadband solar

204   absorption, excellent water transpiration and thermal insulation, which also offered an

205   option for the application in solar evaporation systems with solar concentrators. Above

206   results demonstrated that the upper surface of the PMS possesses the excellent solar

207   evaporation capacity under E_1 illumination.

208   The PMS cylinder can extend its evaporation area to the 3D space to harvest more

209   E_2 in surroundings, attributing to its excellent water-lifting capacity. To evaluate the

210   evaporation capacity of the 3D evaporator, a pre-wetted PMS cylinder ($\approx$ 1.5 cm in

211   diameter) was fixed in the middle of a 100 ml beaker by a foam, with the cylinder

212   bottom immersing in water, as shown in Figure 4C. Then, the evaporation rates of the

213   PMS cylinder at different heights under illumination and the IR image were recorded

214   in Figure 4D and E. Unless other specified, each calculation of evaporation rate was

215   based on the occupied area of the cylinder. Figure 4E shows that the evaporation rates

216   of the PMS evaporator were increased with the height of the cylinder attributing to the

217   increased harvesting of E_2, and reached the maximum at the height of 10-cm-height

218   (10.30 LMH). It can also be confirmed by the evaporation-rate curve of the PMS

219   cylinder system without E_1 illumination (Figure S9). The evaporation rate of the single

220　PMS cylinder is the highest value among the recent reports (Table S2). Correspondingly,

221　the T_{ave} of the upper surface of the 10-cm-height PMS system was maintained at 35.2°C

222　after 60 min illumination, which is consistent with the value in its upper surface

223　experiment. Meanwhile, the T_{ave} of the side surface of the PMS cylinder (17.1°C) was

224　2.8°C lower than the surrounding temperature, indicating that the whole side part of the

225　PMS was continuously capturing the heat energy of E_2 and evaporating during the

226　operation. Besides, the heat conduction loss to bulk water in the upper surface

227　evaporation experiment (10.4%) was utilized by the evaporation of the side surfaces in

228　3D evaporation experiment, thus the utilization of E_1 was also improved at the height

229　of 10 cm. Above results indicate that a reasonable 3D structured evaporator can

230　effectively improve the utilization of both E_1 and E_2, and further increase the flux of

231　water production in solar evaporation.

232　　For comparison, a commercial cotton fiber cylinder as common 3D evaporator with

233　the same diameter (1.5 cm) was also coated by PPy (defined as PCF) for the evaporation

234　test. The maximum evaporation rate of the single PCF was only 2/5 that of PMS

235　cylinder. The reason for the limit evaporation of the cylinders is reasoned that the

236　capillary transport rate cannot satisfy the evaporation rate of the upper surface after

237　reaching a certain height. The decrement of the evaporation after reaching the height is

238　because the upper surface gradually lost its evaporation when the height of the cylinder

239　is above the capillary transport.[40, 41] To further evaluate the water lifting process of each

240　sample, the dry PMS cylinder and PCF cylinder (10-cm-height) were proposed as

241   Figure 4C, respectively. In the initial stage, the temperatures of the cores were in

242   accordance with the surrounding (19.9°C). With the increase of time, the side surfaces

243   of the cylinders were gradually getting dark (16.2°C) due to infiltration and evaporation

244   of water. The PMS cylinder was wholly infiltrated up by water after 180 min, revealing

245   the great potential of transporting water into 3D space. On the contrary, only around

246   1/3 height of the PCF cylinder was wetted by water in the same procedures. It is

247   probably reasoned that the interlaced cotton fibers impeded the further water elevation

248   due to the large aperture and tortuous (Figure S10). The vascular bundle is a tubular

249   structure with no diaphragm, the tortuosity of this capillary-structure is almost 0, which

250   enabled vertical water lifting to a higher level (Detailed in Figure S11). At the same

251   time, regular and horizontal micro-gaps between the cell walls can facilitate the uniform

252   distribution of water to the outside surface of the evaporators for water vaporing.[42] The

253   tortuosity of the whole PMS and PCF was 1.5 and 1.6, respectively (Mercury

254   measurements, Micromeritics AutoPore IV 9510). This combination of the vertical

255   water lifting and horizontal water distribution is the reasoned that PMS achieved a

256   breakthrough in solar water production, which also indicates that the upper limit of

257   evaporation rate can still be raised as long as the structure is properly designed. The

258   durability of the PMS was tested by conducting a recycle experiment for 10 days. The

259   evaporator was irradiated under light for 8 h each day, then totally immersed in the

260   water until the operation of the next day. As observed in Figure S12A, after 10 days of

261   repeat measurement, there was no obvious decrease on the evaporation rate (10.16 ±

0.19 LMH). The PPy on the MS was also stable after 10 days of operation as shown in

263 Figure S12B, indicating the excellent durability.
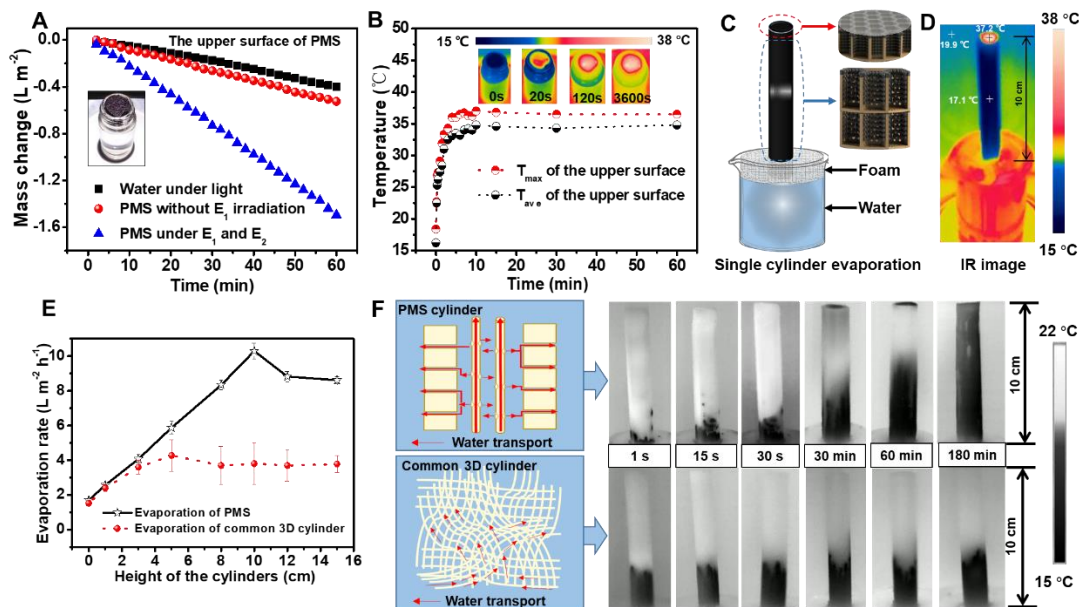
Figure 4. Solar evaporation of a single PMS cylinder. (A) The mass change of the upper layer of the PMS under different intensities of solar illumination. (B) Maximum and average temperatures of surfaces of PMS as a function of time. Inserts show the photograph and IR images of the upper-view over the PMS. The IR photos correspond to t = 0, 20, 50, 100 and 3600 s after illumination. (C) Schematic setup for 3D evaporation capacity test of the PMS. (D) IR image of the 10-cm-height PMS under 1 sun illumination. (E) The evaporation rates of single PMS and common 3D cylinder with different heights. (F) The schematic illustrations and IR images of the water transport process in PMS and common 3D cylinder.

The PMS array presents a superior vapor flux after a reasonable arrangement. In addition to the single PMS cylinder, the evaporation of the PMS array also needs to be tested to verify its scaled-up capacity. As illustrated in Figure 5A, the utilization of the

276   E_1 of a single PMS cylinder in the array was rarely reduced when forming an array,

277   attributing to that the evaporation fields of each upper surface were independent. At the

278   initial state, the surrounding temperature (T_2) obtained through the E_2 was higher than

279   the temperature of the side surface of the PMS cylinder (T_1), which triggered the

280   evaporation of the side surfaces. However, the evaporation at the side surfaces of each

281   PMS cylinder would mutually interfere with each other due to the interaction of their

282   evaporation fields and competing for the utilization of E_2, resulting in the decrement of

283   the evaporation. A reasonable arrangement of the array with optimized distance among

284   each cylinder is required to reduce the disturbance between the evaporation fields of

285   the side surfaces. As shown in the inner images of Figure 5B, a type of the PMS array

286   (3×3) with one side under varying distances (set as x mm) was performed in the solar

287   evaporation experiment, the evaporation rates of which based on the occupied area

288   (with blue appearance) were calculated. When the PMS array is closely aligned, the

289   evaporation rate was calculated to be 2.1 LMH, indicating that the side evaporation still

290   played a role attributing to the space left by the tangent of cylinders. As the distance

291   increases, the water production of the array was enhanced owing to that the E_2 was

292   increased with space increasing (Figure S13). In contrast, the evaporation rates based

293   on the occupied area were varying with the distance increasing, resulting from the

294   sacrifice of E_1 in the blank space. In other words, the increase of the distance between

295   cylinders would lead to increase utilization of the E_2 and decrease utilization of the E_1.

296   As shown in Figure 5B, the curves reached an inflection point at the distance of 15 mm,

17

297 and the maximum evaporation rate (3.0 LMH) of the array was also reached at this

298 point, which is much higher than the early reported arrayed 3D evaporators. The energy

299 enhancement contributed by E_2 of the array (EC_{E2}) at the maximum evaporation rate

300 was calculated through the following express: $EC_{E2} = (R_0 - R_1)/R_1$, where the R_0 is the

301 evaporation of the whole evaporation under both E_1 and E_2, the R_1 is the evaporation

302 under only E_1. Assuming that the E_1 was 100% utilized, the EC_{E2} at the maximum

303 evaporation flux (3.0 LMH) was calculated to be 106 %. It indicates that the

304 contribution of E_2 was at a high level when the PMS cylinders forming an array with a

305 proper arrangement. For comparison, an array with totally independent cylinders was

306 also performed as shown in Figure S14, the maximum evaporation rate of which was

307 only 2.1 LMH. The reason for the great performance of our array is probably due to the

308 more efficient water lifting and transportation (twice speeder than the totally

309 independent array, proved by Figure S15) and more efficient energy utilization. In

310 support of our experimental results, a Comsol model was developed to simulate the

311 evaporation process of the single and the arrayed PMS cylinder. The modeled structure

312 was shown in Figure S16, models with different numbers (n = 1, 3) and distances (x =

313 0, 1, 1.5 cm), stable height (h = 100 mm) and diameter (d = 15mm) were established in

314 a 3D mapping. A simple model of the evaporation of porous media was used to describe

315 the consumption of E_2 (without E_1) around the cylinder during evaporation. The

316 simulation results of the steady-state temperature of the single and arrayed PMS

317 cylinder were presented in Figure 5C. When forming an array, the temperature of the

318　inner space between cylinders (T_2) was varying with the distance changing due to the

319　interaction of each evaporation fields. The temperature of the PMS cylinder (T_1) was

320　stable at 21.6°C, which is 2.4°C lower than the original environment due to the

321　evaporation consumption. When the cylinders were closely aligned, the T_2 in cylinders

322　was about 20.5°C, which is 1.1°C lower than T_1 in the steady-state, which is reasoned

323　that the exchanged and replenished of the E_2 cannot catch up with the rate of

324　evaporation energy consumption at the inner spaces of the array, then resulting in an

325　impediment of the side evaporation. As the distance increased to 15 mm, the T_2

326　recovered to the normal value consistent with T_1 attributing to the increased energy

327　replenishing and exchanging, indicating that the evaporation of the side surfaces of the

328　array can be maintained continuously at this optimized distance. These predicted results

329　were consistent with our experimental result. Above results indicate that the arrayed

330　PMS cylinders with proper arrangement still possessed a superior solar utilization on

331　both E_1 and E_2.

332
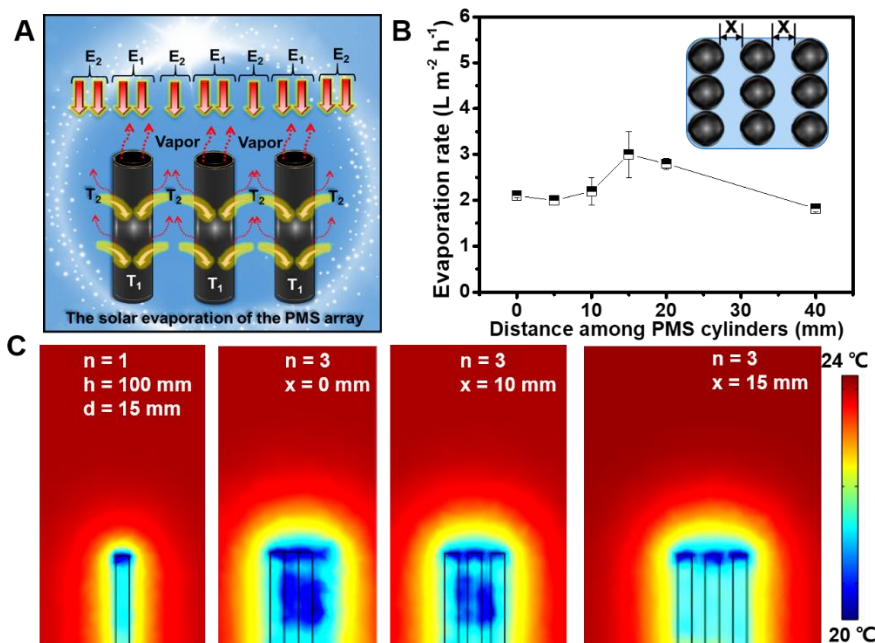
Figure 5. Solar evaporation experiments of a PMS array. (A) The schematic illustration of the solar

evaporation in array. (B) The evaporation rate of our array as function of the distance change among

the PMS cylinders based on the occupied area (with blue appearance). Insets show the photograph

and scheme of the PMS array. (C) The Comsol simulation results about the evaporation of the side

views of the single PMS cylinder and the PMS array.

Outdoor water production. Figure S17 shows the PMS building blocks can

flexibly take advantage of 3D space to increase the area of light absorption and

evaporation as much as possible, whether in traditional flat still, single slope still,

double slope still or semi-circular still. To test the outdoor water distillation capacity of

the PMS building blocks, a typical single slope solar distillation device was designed

as our prototype (Figure 6A and Figure S18A). The devices were placed at the campus

of Harbin Institute of Technology (North latitude 45°) from 10:00 to 16:00 on May 26th,

2018 (Figure 6B). Under nature solar illumination, seawater obtained from Bohai,

346   China (average salinity, 26‰) was transferred to vapor attributing to the heat generation.

347   The solar intensity, outdoor temperature and the inside temperature of the still were

348   recorded in Figure S19. A planar system consisted of PPy paper integrated with

349   insulation foam in the same type of prototype was employed as a comparison system

350   (Figure S19B), the light-to-vapor efficiency (E_1) of which was calculated to be 90%

351   under one-sun. As shown in Figure 6C, the mass of the collected water was increasing

352   with evaporation time and achieved 8.0 L m^{-2} (based on the occupied area of the PMS

353   array) after 6 h of evaporation (average solar flux is 0.55 kW m^{-2}). When the light

354   intensity is normalized to one-sun intensity, we estimate that the amount of pure water

355   collection can reach a record production of 2.2 LMH, which was 4 times higher than

356   that of the planar system, indicating that the utilization of 3D space can significantly

357   improve the water collection flux in the outdoor environment. For comparison, the

358   water production from recently reports in outdoor were also normalized to one-sun

359   intensity and listed in Figure 6D. Besides, there was no salt crystals form on the surface

360   of PMS after one-day of operation. To further prove this the performance, a single PMS

361   was placed in 3.5% NaCl water for 8 h of continuous solar evaporation under one-sun.

362   As shown in Figure S20, the evaporation rate of the PMS was stable at about 8.45kg m^{-2}

363   ^{2} h^{-1} without decrement and no salt crystals on the surface. It is probably reasoned that

364   the evaporator has abundant water transport channels, the movement of ions in the brine

365   during evaporation reaches an equilibrium in these channels.[43-45]

366   As for the water quality, the concentrations of the elements in the initial seawater

367   and the collected fresh water were measured. As shown in Figure 6E, the concentrations

368   of the five primary elements (Na^+, K^+, Ca^{2+}, Mg^{2+} and B^{3+}) presented in the seawater

369   were all below 1 mg L^{-1} after distillation, the decrement of which were more than 98%.

370   The concentration values of elements in the distilled water were far below the standards

371   of the World Health Organization (1000 mg L^{-1}).[46] Notably, the toxic pollutant B^{3+} in

372   seawater, which is hard trapped by conventional reverse osmosis (RO) technology,

373   could be effectively removed (remove rate is 98.32%).[47] Besides, the PMS cylinders

374   could be easily scaled-up as shown in Figure S21, revealing a huge potential for the

375   practical application. Moreover, as a by-product of natural maize agricultural

376   production, the annual yield of MS in China reaches 900 million tons, while the

377   comprehensive utilization of which on average was less than 40%.[48] Therefore, offering

378   a more reasonable way to turn this "waste" into "wealth" also makes a great sense.
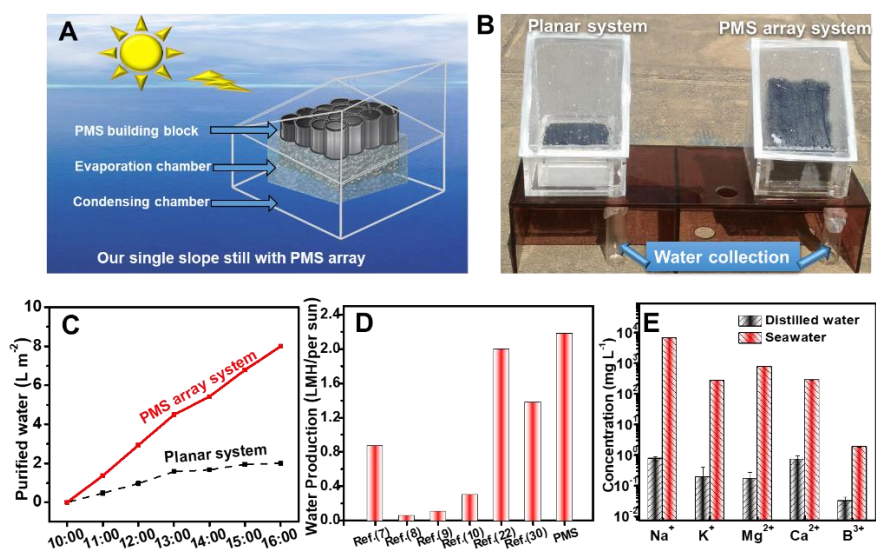
379

380   Figure 6. Outdoor water production. (A) the PMS building blocks in our solar still. (B) The

381   photograph shows the evaporation test of the planar system and PMS system in the outdoor

condition. (C) The amount of the purified water during 6 h of outdoor experiment. (D) Comparison of the outdoor water production of the previous reports under normalized one-sun intensity. (E) The concentration of the elements in seawater and distilled water.

Implications. We have rationally demonstrated a high-water-produced 3D solar evaporator based on a photo-thermal vascular structure to resolve the low water production problem in solar distillation system. The low-tortuosity vascular structures enabled high water lifting vertically and the horizontal micro-gaps transported the water broadly to the 3D space of the evaporators, which contributed to the effective utilization of the heat energy in the surroundings. The state-of-the-art vapor generation rate (3.0 LMH), clean water production capability (2.2 LMH) under one sun condition and fabrication from agricultural by-product make this development more competitive than other solar distillation.

Of course, the water production of the seawater desalination is still at a low level compared to a pump-driven RO system. However, no requirement for pretreatment, post-treatment and additional energy input makes solar distillation simple and inexpensive, hence, it is still a great option for water production and seawater desalination in emergency circumstances or remote rural and island areas. Besides, the effective removal of boron element from seawater is another attractive feature of PMS solar distillation. The present development is also expected to combine with other previous strategies to further enhance the solar distillation, and is believed to be quite meaningful for not only solar desalination, but also solar disinfection, power generation,

403 wastewater volume reduction and so on.

ASSOCIATED CONTENT

Supporting Information

The Supporting Information is available free of charge on the ACS Publications website at DOI:

 Experimental section (PDF)

AUTHOR INFORMATION

Corresponding Author

*E-mail: wangweirs@hit.edu.cn; tangc@hku.hk.

ORCID

Fuyi Cui: 0000-0002-4107-9398

Wei Wang: 0000-0002-0583-0682

Notes

The authors declare no competing financial interest.

ACKNOWLEDGMENTS

REFERENCES

(1) Werber, J. R.; Osuji, C. O.; Elimelech, M., Materials for next-generation desalination and water purification membranes. *Nat. Rev. Mater.* **2016,** *1* (5), 16018.

(2) Tao, P.; Ni, G.; Song, C.; Shang, W.; Wu, J.; Zhu, J.; Chen, G.; Deng, T., Solar-driven interfacial evaporation. *Nature Energy* **2018,** *3* (12), 1031-1041.

(3) Gao, M.; Zhu, L.; Peh, C. K.; Ho, G. W., Solar absorber material and system designs for photothermal water vaporization towards clean water and energy production. *Energ. Environ. Sci.* **2019,** *12* (3), 841-864 .

4) Mei, Y.; Tang, C. Y., Recent developments and future perspectives of reverse electrodialysis technology: A review. *Desalination* **2018,** *425*, 156-174.

(5) Xu, Y.; Xu, H.; Zhu, Z.; Hou, H.; Zuo, J.; Cui, F.; Liu, D.; Wang, W., A mechanically durable, sustained corrosion-resistant photothermal nanofiber membrane for highly efficient solar distillation. *J. Mater. Chem. A* **2019**, 7, (39), 22296-22306.

(6) Loo, S.-L.; Fane, A. G.; Krantz, W. B.; Lim, T.-T., Emergency water supply: a review of potential technologies and selection criteria. *Water Res.* **2012,** *46* (10), 3125-3151.

(7) Lou, J.; Liu, Y.; Wang, Z.; Zhao, D.; Song, C.; Wu, J.; Dasgupta, N.; Zhang, W.; Zhang, D.; Tao, P.; Shang, W.; Deng, T., Bioinspired multifunctional paper-based rgo composites for solar-driven clean water generation. *ACS Appl. Mater. Interfaces* **2016,** *8* (23), 14628-14636.

(8) Liu, Z.; Song, H.; Ji, D.; Li, C.; Cheney, A.; Liu, Y.; Zhang, N.; Zeng, X.; Chen, B.; Gao, J.; Li, Y.; Liu, X.; Aga, D.; Jiang, S.; Yu, Z.; Gan, Q., Extremely cost-effective and efficient solar vapor generation under nonconcentrated illumination using thermally isolated black paper. *Global Chall.* **2017,** *1* (2), 1600003.

(9) Ni, G.; Zandavi, S. H.; Javid, S. M.; Boriskina, S. V.; Cooper, T. A.; Chen, G., A salt-rejecting floating solar still for low-cost desalination. *Energ. Environ. Sci.* **2018,** *11* (6), 1510-1519.

(10) Feng, X.; Zhao, J.; Sun, D.; Shanmugam, L.; Kim, J.-K.; Yang, J., Novel onion-like graphene aerogel beads for efficient solar vapor generation under non-concentrated illumination. *J. Mater. Chem. A* **2019,** *7* (9), 4400-4407.

(11) Xu, Y.; Ma, J.; Han, Y.; Zhang, J.; Cui, F.; Zhao, Y.; Li, X.; Wang, W., Multifunctional CuO Nanowire Mesh for Highly Efficient Solar Evaporation and Water Purification. *ACS Sustain. Chem. Eng.* **2019**, 7, (5), 5476-5485.

(12) Ahsan, A.; Imteaz, M.; Thomas, U. A.; Azmi, M.; Rahman, A.; Nik Daud, N. N., Parameters affecting the performance of a low cost solar still. *Appl. Energy* **2014,** *114*, 924-930.

(13) Sharshir, S. W.; Peng, G.; Wu, L.; Essa, F. A.; Kabeel, A. E.; Yang, N., The effects of flake graphite nanoparticles, phase change material, and film cooling on the solar still performance. *Appl. Energy* **2017,** *191*, 358-366.

(14) Huang, L.; Pei, J.; Jiang, H.; Hu, X., Water desalination under one sun using graphene-based material modified PTFE membrane. *Desalination* **2018,** *442*, 1-7.

(15) Finnerty, C.; Zhang, L.; Sedlak, D. L.; Nelson, K. L.; Mi, B., Synthetic graphene oxide leaf for solar desalination with zero liquid discharge. *Environ. Sci. Technol.* **2017,** *51* (20), 11701-11709.

(16) Shi, Y.; Zhang, C.; Li, R.; Zhuo, S.; Jin, Y.; Shi, L.; Hong, S.; Chang, J.; Ong, C.; Wang, P., Solar evaporator with controlled salt precipitation for zero liquid discharge

desalination. *Environ. Sci. Technol.* **2018,** *52* (20), 11822-11830.

(17) Bae, K.; Kang, G.; Cho, S. K.; Park, W.; Kim, K.; Padilla, W. J., Flexible thin-film black gold membranes with ultrabroadband plasmonic nanofocusing for efficient solar vapour generation. *Nat. Commun.* **2015,** *6*, 10103.

(18) Yang, Y.; Zhao, R.; Zhang, T.; Zhao, K.; Xiao, P.; Ma, Y.; Ajayan, P. M.; Shi, G.; Chen, Y., Graphene-based standalone solar energy converter for water desalination and purification. *ACS nano* **2018,** *12* (1), 829-835.

(19) Song, H.; Liu, Y.; Liu, Z.; Singer, M. H.; Li, C.; Cheney, A. R.; Ji, D.; Zhou, L.; Zhang, N.; Zeng, X.; Bei, Z.; Yu, Z.; Jiang, S.; Gan, Q., Cold vapor generation beyond the input solar energy limit. *Adv. Science* **2018,** *5* (8), 1800222.

(20) Wang, J.; Li, Y.; Deng, L.; Wei, N.; Weng, Y.; Dong, S.; Qi, D.; Qiu, J.; Chen, X.; Wu, T., High-performance photothermal conversion of narrow-bandgap Ti_2O_3 nanoparticles. *Adv. Mater.* **2017,** *29* (3), 1603730.

(21) Lin, X.; Chen, J.; Yuan, Z.; Yang, M.; Chen, G.; Yu, D.; Zhang, M.; Hong, W.; Chen, X., Integrative solar absorbers for highly efficient solar steam generation. *J. Mater. Chem. A* **2018,** *6* (11), 4642-4648.

(22) Zhao, F.; Zhou, X.; Shi, Y.; Qian, X.; Alexander, M.; Zhao, X.; Mendez, S.; Yang, R.; Qu, L.; Yu, G., Highly efficient solar vapour generation via hierarchically nanostructured gels. *Nat. Nanotechnol.* **2018,** *13* (6), 489-495.

(23) Zhou, X. Y.; Zhao, F.; Guo, Y. H.; Rosenberger, B.; Yu, G. H., Architecting highly hydratable polymer networks to tune the water state for solar water purification. *Sci. Adv.* **2019,** *5*, (6), eaaw5484.

(24) Zhou, X.; Guo, Y.; Zhao, F.; Yu, G., Hydrogels as an Emerging Material Platform for Solar Water Purification. *Acc. Chem. Res.* **2019**, 52, (11), 3244-3253.

(25) Guo, Y.; Zhou, X.; Zhao, F.; Bae, J.; Rosenberger, B.; Yu, G., Synergistic energy nanoconfinement and water activation in hydrogels for efficient solar water desalination. *ACS nano* **2019**, 13, (7), 7913-7919.

(26) Guo, Y.; Zhao, F.; Zhou, X.; Chen, Z.; Yu, G., Tailoring Nanoscale Surface Topography of Hydrogel for Efficient Solar Vapor Generation. *Nano Lett.* **2019**, 19, (4), 2530-2536.

(27) Lewis, N. S., Research opportunities to advance solar energy utilization. *Science* **2016,** *351* (6271), aad1920.

(28) Xu, N.; Hu, X.; Xu, W.; Li, X.; Zhou, L.; Zhu, S.; Zhu, J., Mushrooms as efficient solar steam-generation devices. *Adv. Mater.* **2017,** *29* (28), 1606762.

(29) Li, X.; Lin, R.; Ni, G.; Xu, N.; Hu, X.; Zhu, B.; Lv, G.; Li, J.; Zhu, S.; Zhu, J., Three-dimensional artificial transpiration for efficient solar waste-water treatment. *Natl. Sci. Rev.* **2018,** *5* (1), 70-77.

(30) Shi, Y.; Li, R.; Jin, Y.; Zhuo, S.; Shi, L.; Chang, J.; Hong, S.; Ng, K.-C.; Wang, P., A 3D Photothermal Structure toward Improved Energy Efficiency in Solar Steam Generation. *Joule* **2018,** *2* (6), 1171-1186.

(31) Li, X.; Li, J.; Lu, J.; Xu, N.; Chen, C.; Min, X.; Zhu, B.; Li, H.; Zhou, L.; Zhu, S.;

Zhang, T.; Zhu, J., Enhancement of interfacial solar vapor generation by environmental energy. *Joule* **2018**, *2* (7), 1331-1338.

(32) Deng, Z.; Miao, L.; Liu, P.-F.; Zhou, J.; Wang, P.; Gu, Y.; Wang, X.; Cai, H.; Sun, L.; Tanemura, S., Extremely high water-production created by a nanoink-stained PVA evaporator with embossment structure. *Nano Energy* **2019**, *55*, 368-376.

(33) Wu, X.; Wu, L.; Tan, J.; Chen, G. Y.; Owens, G.; Xu, H., Evaporation above a bulk water surface using an oil lamp inspired highly efficient solar-steam generation strategy. *J. Mater. Chem. A* **2018**, *6* (26), 12267-12274.

(34) Zhu, M.; Li, Y.; Chen, G.; Jiang, F.; Yang, Z.; Luo, X.; Wang, Y.; Lacey, S. D.; Dai, J.; Wang, C., Tree-inspired design for high-efficiency water extraction. *Adv. Mater.* **2017**, *29* (44), 1704107.

(35) Zhu, M.; Li, Y.; Chen, F.; Zhu, X.; Dai, J.; Li, Y.; Yang, Z.; Yan, X.; Song, J.; Wang, Y.; Hitz, E.; Luo, W.; Lu, M.; Yang, B.; Hu, L., Plasmonic wood for high-efficiency solar steam generation. *Adv. Energy Mater.* **2018**, *8* (4), 1701028.

(36) Liu, K. K.; Jiang, Q.; Tadepalli, S.; Raliya, R.; Biswas, P.; Naik, R. R.; Singamaneni, S., Wood-graphene oxide composite for highly efficient solar steam generation and desalination. *ACS Appl. Mater. Interfaces* **2017**, *9* (8), 7675-7681.

(37) Yuan, L.; Yao, B.; Hu, B.; Huo, K.; Chen, W.; Zhou, J., Polypyrrole-coated paper for flexible solid-state energy storage. *Energ. Environ. Sci.* **2013**, *6* (2), 470-476.

(38) Wang, W.; You, S.; Gong, X.; Qi, D.; Chandran, B. K.; Bi, L.; Cui, F.; Chen, X., Bioinspired nanosucker array for enhancing bioelectricity generation in microbial fuel cells. *Adv. Mater.* **2016**, *28* (2), 270-275.

(39) Jin, H.; Lin, G.; Bai, L.; Zeiny, A.; Wen, D., Steam generation in a nanoparticle-based solar receiver. *Nano Energy* **2016**, *28*, 397-406.

(40) Lu, N.; Likos, W., Rate of capillary rise in soil. *J Geotech. Geoenviron.* **2004**, 130, (6), 646-650.

(41) Rajagopalan, D.; Aneja, A. P.; Marchal, J.-M., Modeling capillary flow in complex geometries. *Text. Res. J.* **2001**, *71*, (9), 813-821.

(42) Maurel, C.; Chrispeels, M. J., Aquaporins. A molecular entry into plant water relations. *Plant Physiol.* **2001**, *125* (1), 135-8.

(43) Xu, Y.; Liu, D.; Xiang, H.; Ren, S.; Zhu, Z.; Liu, D.; Xu, H.; Cui, F.; Wang, W., Easily scaled-up photo-thermal membrane with structure-dependent auto-cleaning feature for high-efficient solar desalination. *J. Membrane Sci.* **2019**, 586, 222-230.

(44) Zhou, X.; Zhao, F.; Guo, Y.; Zhang, Y.; Yu, G., A hydrogel-based antifouling solar evaporator for highly efficient water desalination. *Energ. Environ. Sci.* **2018**, 11, (8), 1985-1992.

(45) Kuang, Y.; Chen, C.; He, S.; Hitz, E. M.; Wang, Y.; Gan, W.; Mi, R.; Hu, L., A High-Performance Self-Regenerating Solar Evaporator for Continuous Water Desalination. *Adv. Mater.* **2019**, 31, (23), e1900498.

(46) https://www.who.int/water_sanitation_health/publications/desalination_guidance.

(47) Tu, K. L.; Nghiem, L. D.; Chivas, A. R., Boron removal by reverse osmosis

550 membranes in seawater desalination applications. *Sep. Purif. Technol.* **2010,** *75* (2), 87-
551 101.
552 (48) https://www.sohu.com/a/145506749_488938.